The Astrophysical Journal, 823:159 (12pp), 2016 June 1
doi:10.3847/0004-637X/823/2/159

AN OPTICALLY THICK DISK WIND IN GRO J1655–40?

M. Shidatsu[1], C. Done[2], and Y. Ueda[3]
[1] MAXI Team RIKEN, 2-1 Hirosawa, Wako, Saitama 351-0198, Japan; megumi.shidatsu@riken.jp
[2] Centre for Extragalactic Astronomy Department of Physics, University of Durham, South Road, Durham, DH1 3LE, UK
[3] Department of Astronomy, Kyoto University, Kitashirakawa-Oiwake-cho, Sakyo-ku, Kyoto 606-8502, Japan
Received 2015 December 6; accepted 2016 April 14; published 2016 June 1

ABSTRACT

We revisited the unusual wind in GRO J1655−40, detected with *Chandra* in 2005 April, using long-term *Rossi X-ray Timing Explorer* X-ray data and simultaneous optical/near-infrared photometric data. This wind is the most convincing case for magnetic driving in black hole binaries, as it has an inferred launch radius that is a factor of 10 smaller than the thermal wind prediction. However, the optical and near-infrared (OIR) fluxes monotonically increase around the *Chandra* observation, whereas the X-ray flux monotonically decreases from 10 days beforehand. Yet the optical and near-infrared fluxes are from the outer, irradiated disk, so for them to increase implies that the X-rays likewise increased. We applied a new irradiated disk model to the multi-wavelength spectral energy distributions. Fitting the OIR fluxes, we estimated the intrinsic luminosity at the *Chandra* epoch was $\gtrsim 0.7 L_{\rm Edd}$, which is more than one order of magnitude larger than the observed X-ray luminosity. These results could be explained if a Compton-thick, almost completely ionized gas was present in the wind and strong scattering reduced the apparent X-ray luminosity. The effects of scattering in the wind should then be taken into account for discussion of the wind-driving mechanism. Radiation pressure and Compton heating may also contribute to powering the wind at this high luminosity.

Key words: accretion, accretion disks – black hole physics – X-rays: binaries – X-rays: individual (GRO J1655–40)

1. INTRODUCTION

Since the first detection of highly ionized absorption lines in the late 1990s, high-resolution X-ray spectroscopy has provided great opportunities to probe disk winds in black hole (BH) and neutron star (NS) low-mass X-ray binaries (e.g., Ueda et al. 1998, 2001, 2009; Kotani et al. 2000; Boirin & Parmer 2003; Díaz Trigo et al. 2006, 2014; Miller et al. 2006, 2008; Kubota et al. 2007). Disk winds are thought to have an equatorial structure, extending along the disk plane with a relatively small solid angle, because the lines are only seen in systems with high inclination angles larger than ≈60° (Ponti et al. 2012) and do not show large orbital dependence of variability (Yamaoka et al. 2001). The high mass-loss rates, comparable to or even an order of magnitude larger than the mass accretion rates (Ueda et al. 2010; Neilsen et al. 2011), suggest that disk winds play a key role in the dynamics of accretion onto compact objects, although how and how much they affect the accretion disks have been poorly understood.

There are three major mechanisms proposed for powering the disk winds in low-mass X-ray binaries: radiation pressure, thermal pressure (due to Compton heating), and magnetic processes. Radiation pressure works effectively at near- or super-Eddington luminosity, if gas is highly ionized. Thermal winds can be launched from anywhere above a certain radius at which the isothermal sound speed of gas heated by X-rays overcomes the local escape velocity. This radius, called the "Compton radius" ($R_{\rm C}$), is given by

$$R_{\rm C} \approx 10^{10} \left(\frac{M_{\rm BH}}{M_{\odot}}\right) \left(\frac{T_{\rm C}}{10^8\ {\rm K}}\right)^{-1} {\rm cm}, \quad (1)$$

where $M_{\rm BH}$ and $T_{\rm C}$ are the BH mass and Compton temperature, respectively. More detailed calculations suggest that the thermal winds can be launched from smaller radii, $\gtrsim 0.1\ R_{\rm C}$ (Begelman et al. 1983; Woods et al. 1996), which correspond to 10^4–$10^5\ R_{\rm g}$ ($R_{\rm g}$ is the gravitational radius: $GM_{\rm BH}/c^2$) in stellar-mass BH X-ray binaries. Ionized gas located within $R_{\rm C}$ remains bound to the surface of the accretion disks as hot atmosphere.

Since a wind is photoionized by X-ray radiation, its launching radius R can be observationally estimated from the ionization parameter ξ defined as,

$$\xi = \frac{L_{\rm X}}{nR^2}, \quad (2)$$

where $L_{\rm X}$ and n represent the ionizing luminosity and the number density of the wind, respectively. Constraining n directly is often not easy, and in such cases, the column density of the wind ($N_{\rm H} \sim n\Delta R$, where ΔR is the length of the wind) has been used under the assumption $\Delta R \sim R$ to derive R through the above equation (e.g., Ueda et al. 1998; Kotani et al. 2000; Kubota et al. 2007). Díaz Trigo & Boirin (2013) showed that outflowing and static ionized absorbers in NS X-ray binaries have R values consistent with the thermal driven winds and atmosphere, respectively. Many winds detected in BH X-ray binaries are also consistent with the thermal and/or radiation-pressure-driven winds (e.g., Kotani et al. 2000; Kubota et al. 2007; Neilsen & Lee 2009; Díaz Trigo et al. 2014). The wind velocities are about 100–1000 km $\rm s^{-1}$, in agreement with the prediction that the winds are generated in the outer parts of the disks.

In 2005, a remarkable wind from GRO J1655−40 was detected with the *Chandra* High Energy Transmission Grating (HETG) (Miller et al. 2006, 2008; Netzer 2006). The observed spectrum exhibited a rich forest of blueshifted ionized absorption lines. The estimated intrinsic luminosity (0.03 $L_{\rm Edd}$[4]) is not very high and hence the wind cannot be powered

---

[4] $L_{\rm Edd}$ (Eddington Luminosity) = $1.5 \times 10^{38} (M_{\rm BH}/M_{\odot})$ erg $\rm s^{-1}$ for the solar abundances.

by radiation pressure. The thermal wind interpretation is also difficult because this luminosity is just about the critical luminosity ($L_{\rm crit} \approx 0.03 L_{\rm Edd}$; Begelman et al. 1983) below which the Compton heating is not efficient enough to drive a thermal wind.

As the result of detailed photoionization modeling, the GRO J1655−40 wind was found to have an ionization parameter of $\xi \sim 10^4$ erg cm s^{-1}. The density was directly estimated to be $n \sim 10^{14}$ cm^{-3} from a density-sensitive line ratio of Fe XXII. By using Equation (2), the radius was derived to be $R = 10^{9.7}$ cm, which is one order of magnitude smaller than the radius at which thermal driven winds can form. The disk wind was thus explained by the remaining scenario, i.e., a magnetic driven wind, although the observed outflow velocity ($\approx$1000 km s^{-1}) is lower than the local escape velocity at a radius of $\lesssim 10^{9.7}$ cm ($\gtrsim$4000 km s^{-1}) and seems too low to drive a wind unless it has a much larger velocity in the perpendicular direction.

Recently, Uttley & Klein-Wolt (2015) have found that unusual properties in X-ray short-term variability and continuum spectra were seen around the *Chandra* observation, from a comprehensive study of *Rossi X-ray Timing Explorer* (*RXTE*) data, covering almost the entire outburst episode in 2005. When a deep absorption structure emerged at ~8 keV, the hard X-ray flux was greatly reduced and a very soft X-ray spectrum appeared. The peculiar spectral shape was similar to that of the "hypersoft state" sometimes observed in the high-mass X-ray binary Cyg X-3, which has a massive stellar wind from its Wolf–Rayet companion (e.g., Koljonen et al. 2010). Meanwhile, the variability power above ~0.1 Hz was gradually reduced as the observed X-ray flux decreased. They suggested that these behaviors are linked to the evolution of the disk wind or the accretion flow structure, yet the exact relations among them are still not completely clear.

In this article, we focus on the shape of the multi-wavelength spectral energy distribution (SED) of GRO J1655−40 and its evolution around the *Chandra* observation during the outburst, and reconsider the wind in the context of the long-term behavior of the accretion disk structure. We use the *RXTE* X-ray data and also simultaneous optical and near-infrared (OIR) photometric data from the SMARTS (the Small and Medium Aperture Research Telescope System). The OIR emission can be regarded as a reference of the intrinsic luminosity at the outermost part of the accretion disk, which would be less affected by reprocessing in the wind. The multi-wavelength SEDs thus allow us to connect the properties of inner and outer disks.

In Section 2, we study the long-term X-ray and OIR behavior around the *Chandra* observation. In Section 3, we analyze the multi-wavelength SED at the *Chandra* epoch using a new irradiated disk model, and compare the result with that in the normal high/soft state. Compiling all these results, we discuss the nature of the wind in Section 4. We used HEASOFT version 6.13 to reduce and analyze the data. In the following sections, errors represent the 90% confidence range for a single parameter, unless otherwise stated. Throughout the article, we refer to the table given by Wilms et al. (2000) for the solar abundances. The distance and inclination angle of GRO J1655−40 are assumed to be $D = 3.2$ kpc (Hjellming & Rupen 1995; Orosz & Bailyn 1997) and $i = 70°$ (Greene et al. 2001), respectively.

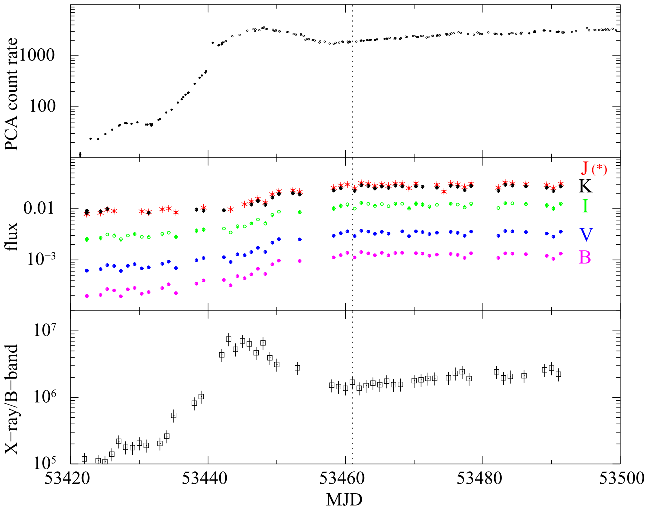

Figure 1. Top: long-term *RXTE*/PCA light curve of GRO J1655−40 in the X-ray band. Middle: optical and near-infrared light curves obtained with SMARTS in *B* (pink), *V* (blue), *I* (green), *J* (red, marked with asterisks), and *K* (black) bands. Bottom: the ratios of the observed *B*-band fluxes with respect to X-ray count rates. The PCA count rates are estimated from the Standard 2 data of the Proportional Counter Array 2 (PCU2) in the full energy band. The SMARTS data are plotted in units of Jy and not corrected for interstellar extinction. The dotted line indicates MJD 53461, corresponding to the *Chandra* observation.

2. LONG-TERM TRENDS IN OPTICAL, NEAR-INFRARED, AND X-RAY PROPERTIES

Figure 1 shows the long-term X-ray and optical/NIR behavior in the first ~80 days of the outburst in 2005, including the date of the *Chandra* observation (April 1 = MJD 53461). The X-ray count rates are obtained with the *RXTE*/Proportional Counter Array (PCA), and the OIR fluxes are taken from the SMARTS photometric observations in the *B*, *V*, *I*, *J*, and *K* bands (see Buxton et al. 2005 and Migliari et al. 2007 for details of the observations).

The most remarkable point is that the OIR fluxes were monotonically increasing in the whole period, while the X-ray flux was decreasing before the *Chandra* epoch. This cannot be explained by an increase of the mass accretion rate alone. As noticed from the bottom panel of Figure 1, the ratio between the X-ray and *B*-band fluxes marks the minimal value at around the *Chandra* observation after the hard-to-soft transition at ~MJD 53440. We note that, among the 5 OIR bands, the *B*-band flux should have the least fractional contribution of the blackbody emission from the companion (an F6-III-type star with a temperature of ≈6300 K; Shahbaz et al. 1999) and is dominated by the irradiated disk emission from the outer disk (see Section 3 for more details).

Using the OIR fluxes and simultaneous *RXTE*/PCA and High Energy X-ray Timing Experiment (HEXTE) data, we created multi-wavelength SEDs in the individual MJDs. We employed the standard data-reduction procedure described in the *RXTE* cookbook and extracted the PCA spectra from the "Standard 2" data of the Proportional Counter Array 2 (PCA2) and the HEXTE spectra from Clusters A and B data for each observation ID. The OIR magnitudes were converted to fluxes, from which we produced spectra and response matrix files in the XSPEC format utilizing the ftool flx2xsp. We added a 0.5% systematic error to each bin in the PCA spectra, following

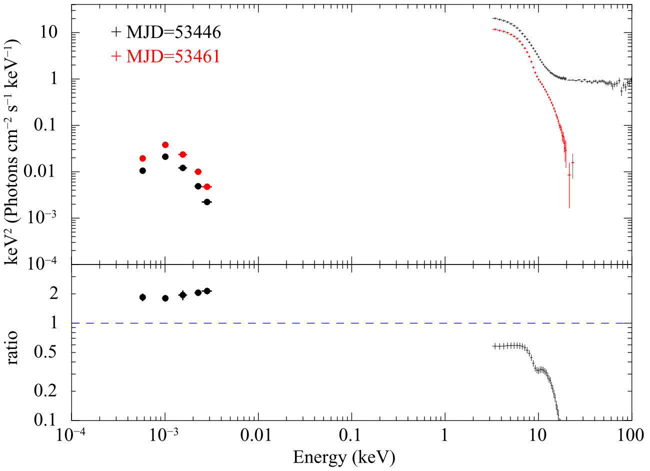

Figure 2. Top: multi-wavelength SEDs in the normal high/soft state (MJD 53446, black) and at the *Chandra* epoch in the hypersoft state (MJD 53461, red). For the HEXTE data (above 20 keV), the Cluster A spectra are not plotted for illustrative purposes. Bottom: the ratio of the two SEDs. The latter data are divided by the former.

previous works (e.g., Migliari et al. 2007; Uttley & Klein-Wolt 2015).

In Figure 2, the SED on MJD 53461, the date of the *Chandra* observation, is compared with that on MJD 53446 in the normal high/soft state, whose X-ray spectrum is well described by a multi-color disk (MCD) combined with a hard tail with a photon index of ≈2. Note that MJD 53446 corresponds to the peak of the observed X-ray flux in the initial outburst rise. This figure shows that the X-ray flux levels decreased at all energies from MJD 53446 to the *Chandra* epoch, whereas the OIR fluxes increased.

Moreover, a huge difference is present in the hard X-ray band. The difference is not just in normalization. The hard tail in the normal high/soft state is suppressed in the spectrum on MJD 53461, which is dominated by the soft X-ray fluxes below 10 keV. As reported by Uttley & Klein-Wolt (2015), this X-ray spectrum can be described with an MCD plus an unusually steep power-law component with a photon index of >5. This peculiar hypersoft state was steadily seen from a few days before the *Chandra* observation, after making rapid and frequent transitions between the normal high/soft and hypersoft states in the preceding ≈10 days. We note that, in Figure 2, a significant depression is present at ≈8 keV in the SED on MJD 53461, which is likely an ionized iron-K edge along with absorption lines produced by the disk winds. This feature was always visible during the hypersoft state and deepened without significant energy shifts as the observed X-ray flux decreased (see Uttley & Klein-Wolt 2015).

As noticed in the bottom panel of Figure 2, the flux ratio of the two observations is almost constant in the soft X-ray band below ∼5 keV, where the disk blackbody dominates. This indicates that the apparent disk luminosity ($L_{\rm disk}$) decreased without significantly changing the inner disk temperature ($T_{\rm in}$). In fact, the hypersoft state produces a vertical branch in the $T_{\rm in}$ versus $L_{\rm disk}$ diagram (see Figure 16 in Done et al. 2007). This means that the evolution of the disk spectrum in the hypersoft state deviates from the standard $L_{\rm disk} \propto T_{\rm in}^4$ relation.

What is unusual in the hypersoft state is not only the characteristics of the SED but also fast X-ray variability. As reported by Uttley & Klein-Wolt (2015), the high-frequency part of the flat noise component was remarkably reduced in the hypersoft state, compared with that in the normal high/soft state. The break frequency in the high/soft state was located at ≈5 Hz, whereas during the hypersoft state it moved to lower frequencies with decreasing X-ray flux to reach ≈0.1 Hz at the *Chandra* observation. They also found that the energy dependence of the PDS shape was not strong, suggesting that the decline of the high-frequency variability was not simply caused by the disappearance of the power-law tail.

3. A NEW IRRADIATED DISK MODEL “OPTXRPLIR” AND ITS APPLICATION TO THE SEDS

Here we model the multi-wavelength SEDs of GRO J1655−40 in the normal soft state and at the *Chandra* epoch in the hypersoft state to test the possibility that the peculiar behaviors in the hypersoft state are associated with the disk wind. Using the OIR data as a reference for the intrinsic emission from the outermost disk region, we investigate whether and how much the disk wind can affect the intrinsic X-ray emission at the *Chandra* epoch.

3.1. The `optxrplir` *Model*

Different spectral components (the companion star, the outer parts of the accretion disk, the synchrotron radiation from the jets, or the hot accretion flow) can contribute to the OIR emission of BH X-ray binaries (see, e.g., van Paradijs 1981, Gierliński et al. 2008, and Gierliński et al. 2009 for contribution from outer disks; Corbel & Fender 2002, Hynes et al. 2003, Buxton & Bailyn 2004, Russell et al. 2007, and Gandhi et al. 2010 for that from jets; and Poutanen & Veledina 2014, Poutanen et al. 2014, and Veledina et al. 2015 for that from hot flows). Normally, jet emission does not contribute in the disk-dominant states. In fact, Migliari et al. (2007) found that the radio flux actually dropped down to an undetectable level and that jets were quenched in the hypersoft state. Usually, the outer disk emission is the major contributor in outbursting BH X-ray binaries with a low-mass companion. The outer disk region is illuminated by X-rays from the inner disk and the Comptonized corona and consequently the reprocessed emission enhances the OIR fluxes. To determine the accurate mass accretion rates through the inner and outer disks, we have to account for the intrinsic disk and Compton-scattered and reprocessed emission components in a self-consistent manner.

For this purpose, we use a new irradiated disk model named “`optxrplir`” and apply it to the multi-wavelength SEDs. This model is based on the `optxirr` model (Sutton et al. 2014), which combines the two models implemented in XSPEC: “`optxagnf`” (Done et al. 2012), the energetically coupled disk plus Comptonized corona model including color temperature correction, and the irradiated disk model “`diskir`” (Gierliński et al. 2008, 2009). Using our new model, we can fully consider the emissions from the inner and outer disk self-consistently.

The main difference between `optxirr` and our model, `optxrplir`, is the radial dependence of the X-ray flux irradiating the disk. The `optxrplir` model assumes that the illuminating flux does not scale with radius as r^{-2}, but $r^{-12/7}$. The reprocessed component in this model is thus more enhanced in the outermost parts of the disk than in the previous models. This radial dependence is derived from a more realistic calculation by solving the hydrostatic and energy balance at each radius of a geometrically thin irradiated disk (Cunningham 1976). In this condition, the disk height increases at larger radii in proportion to $r^{9/7}$ due to heating by irradiation. The $r^{-12/7}$ dependence was recently adopted to model multi-wavelength SEDs in the low/hard state (Veledina et al. 2013). Also, previous irradiated disk models describe the strength of the reprocessed component with one parameter $F_{\rm out}$ (the fraction of illuminating flux thermalized in the outer disk), while `optxrplir` separates it, for the convenience of calculation, into two explicit parameters: the geometry-dependent factor, $f_{\rm out}$, and $(1 - a_{\rm out})$, where $f_{\rm out}$ is the height of the disk at the outer edge divided by the outer radius and $a_{\rm out}$ is the albedo of the outer disk. We assume that the total X-rays, not only hard X-rays, are responsible for reprocessing. This is consistent with the OIR SEDs not largely changing in spite of the huge difference in the hard X-ray tail between the high/soft state and the hypersoft state.

The model includes two different Comptonization components similar to the `optxagnf` model. One is a power-law component extending to the hard X-ray band above 10 keV, which can be used to model the hard tail observed in the normal high/soft state. The other is a low-temperature thermal Comptonization component, which can be used for the steep power-law component sometimes seen at slightly higher energies than an MCD component (e.g., Frontera et al. 2001; Ibragimov et al. 2005; Nakahira et al. 2012). We adopt the latter to model the steep power-law component in the hypersoft state. The former component (hereafter referred to as the "power-law tail") is described with a photon index and a cut-off energy and the latter (the "soft thermal Comptonization component") with an electron temperature ($kT_{\rm e}$) and an optical depth (τ). The `optxrplir` model assumes that the power-law tail is generated from the gravitational energy dissipated within the radii from the innermost stable circular orbit (ISCO) to $R_{\rm pl}$ and that the soft thermal Comptonization component is produced between $R_{\rm pl}$ and $R_{\rm cor}$. Only disk blackbody emission (including irradiation) is emitted from radii larger than $R_{\rm cor}$. The rest of the parameters in the model are all taken from the `optxagnf` model (the BH mass and spin, the distance to the system, and the Eddington ratio) and the `diskir` model (the outer disk radius $R_{\rm out}$, and also $f_{\rm out}$ and $a_{\rm out}$, as explained above).

3.2. SED Analysis with **Optxrplir**

3.2.1. Model Setup

To analyze our multi-wavelength SEDs of GRO J1655−40, we use `optxrplir` as a full model of the irradiated disk emission and its Comptonization. The OIR fluxes also include the blackbody emission from the companion star, for which we use the `bbodyrad` model. Throughout the SED analysis, we fixed the temperature and radius of the companion star to 6300 K and 5.0 $R_\odot$, respectively, and the BH mass at 6.3 $M_\odot$, following the previous estimation by Shahbaz et al. (1999) and Greene et al. (2001). The interstellar X-ray absorption is taken into account by multiplying the `tbabs` model (Wilms et al. 2000). We adopt $N_{\rm H} = 7.4 \times 10^{21}$ cm^{-2} (Miller et al. 2006; Takahashi et al. 2008) as the column density of the Galactic absorption. The extinction of the OIR fluxes is also considered by combining the `redden` model in which the ratio of galactic extinctions $R_V = A_V/(A_V - A_B) = 3.1$ and the interstellar reddening $E(B - V) = 1.26$ are assumed. The value of $E(B - V)$ is derived from $N_{\rm H}$ and the relation $N_{\rm H}/E(B - V) = 5.8 \times 10^{21}$ cm^{-2} mag^{-1}, determined by Bohlin et al. (1978).

The `optxrplir` model assumes an inclination of 60° in calculating the disk spectrum. To incorporate the inclination dependence of the disk emission, we set the normalization to $\cos i/\cos 60^\circ$ ($\approx$0.684, in the case of GRO J1655−40 with $i = 70^\circ$). In addition, this model does not include relativistic smearing. Following Done et al. (2013), we consider this effect by convolving our model with `kerrconv` (Brenneman & Reynolds 2006). The `kerrconv` model uses a_*, i, inner and outer radii (in units of the ISCO radius: $R_{\rm ISCO}$) within which the relativistic effects are considered, the radial emissivity indices of the inner and outer parts, and the break radius (in units of $R_{\rm g}$) at which the emissivity index changes. We link a_* in `kerrconv` to that in `optxrplir` and fix i at 70° and the emissivity indices at 3. The inner and outer radii are set to $1R_{\rm ISCO}$ and $2R_{\rm ISCO}$, respectively. In this way, we convolve the entire disk spectrum with a smearing kernel calculated from the radii between $1R_{\rm ISCO}$ and $2R_{\rm ISCO}$, in which a large fraction of the disk flux is produced[5], instead of integrating the smeared blackbody spectrum at each radius. As shown in Done et al. (2013), the kerrconv*`optx` model with this parameter setting gives a good approximation of relativistic disk models.

3.2.2. SED Fits for the Normal High/Soft State

We first apply this model, "`tbabs*redden(kerrconv*optxrplir+bbodyrad)`," to the multi-wavelength SED on MJD 53446 in the normal high/soft state. Since X-ray spectra in that state typically have a power-law tail but no significant thermal Comptonization component, here we ignore the soft thermal Comptonization component in `optxrplir` (i.e., $R_{\rm pl}$ is linked to $R_{\rm cor}$). As for irradiation, the strength of the reprocessed component is scaled with $F_{\rm out} = f_{\rm out} * (1 - a_{\rm out})$ and it is difficult to constrain both $a_{\rm out}$ and $f_{\rm out}$ simultaneously in spectral fitting. Here, we assume $f_{\rm out} = 0.1$ and leave $a_{\rm out}$ as a free parameter to absorb uncertainties in the geometry of the outer disk. The Eddington ratio ($L/L_{\rm Edd}$), BH spin a_*, the photon index (Γ), and $R_{\rm pl}$ of the power-law tail are also allowed to vary. The cut-off energy of the power-law tail is set to be 1000 keV, a sufficiently high value compared with the energy range of the *RXTE* data. $R_{\rm out}$ is fixed at $10^{5.67}R_{\rm g}$ (4.4×10^{11} cm), which is the tidal radius of GRO J1655−40 given in Shahbaz et al. (1998).[6] We extend the energy range to 10^{-4} keV–1000 keV in the following spectral fit because `kerrconv` is a convolution model.

The left panel of Figure 3 shows the results of the fit for MJD 53446. The model reproduces both the OIR fluxes and the X-ray spectrum, yielding $\chi^2/{\rm dof} = 99/105$. The free parameters are constrained to be $L/L_{\rm Edd} = 0.1370^{+0.005}_{-0.006}$,

---

[5] The choice of the outer radius for the `kerrconv` model does not substantially affect our results. In the case of a Schwarzschild BH, $\gtrsim$10% of the total disk emission is produced between $1R_{\rm ISCO}$ and $2R_{\rm ISCO}$ (Novikov & Thorne 1973; the percentage is slightly larger for $a_* \neq 0$). We confirm that the results of the spectral fits remain unchanged within the 90% error ranges when we adopt 5 $R_{\rm ISCO}$ and 10 $R_{\rm ISCO}$ (below which $\gtrsim$50% and $\gtrsim$70% of the flux are generated, respectively) as the outer radius.

[6] This value corresponds to 80% of the Roche lobe size. To test a different value, we leave $R_{\rm out}$ as a free parameter in the fit of the SED on MJD 53446 and use the best-fit value to fit the SED at the *Chandra* epoch. We confirm that this does not affect our conclusions.

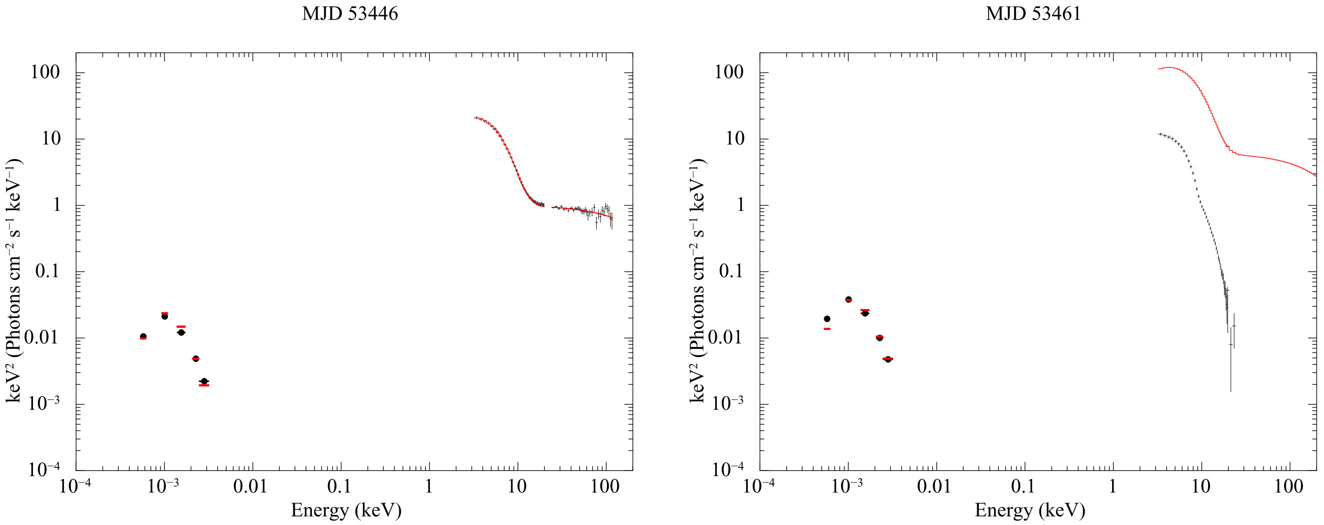

Figure 3. Left: the SED and best-fit `optxrplir+bbodyrad` model in the normal high/soft state (MJD 53446). Right: the SED at the *Chandra* epoch (MJD 53461) plotted with the same model except for the luminosity, which is adjusted to fit the flux levels in the OIR bands.

$a_* = 0.76 \pm 0.03$, $R_{\rm pl} = 4.8 \pm 0.2 R_{\rm g}$, $\Gamma = 2.04 \pm 0.02$, and $a_{\rm out} = 0.974 \pm 0.03$. The strength of the irradiated disk component is thus estimated to be $F_{\rm out} = (2.6 \pm 0.3) \times 10^{-3}$. We note that the high $a_{\rm out}$ value for $f_{\rm out} = 0.1$ is consistent with a highly ionized and reflective disk surface suggested by van Paradijs (1981, 1983) and Gierliński et al. (2009), but combinations of somewhat smaller $a_{\rm out}$ and smaller $f_{\rm out}$ (where $f_{\rm out} > 2.3 \times 10^{-3}$) also may be possible.

The best-fit model corrected for the interstellar absorption/extinction is plotted in Figure 4. It has a double-humped profile unlike the `diskir` model, which instead produces a flat "shoulder" in the νF_ν form. This demonstrates the difference in radial dependence of the disk temperature. We find that the OIR fluxes are dominated by reprocessed emission from the outer edge of the disk irradiated by X-rays. The OIR bands are located at slightly lower frequencies than that of the peak in the reprocessed component, above and below which the relations between the incident X-ray luminosity ($L_{\rm X}$) and the luminosity of the irradiated outer disk ($L_{\nu,\rm ir}$) are given as $L_{\nu,\rm ir} \propto L_{\rm X}^{7/6}$ and $L_{\nu,\rm ir} \propto L_{\rm X}^{1/4}$, respectively (see, e.g., Coriat et al. 2009).

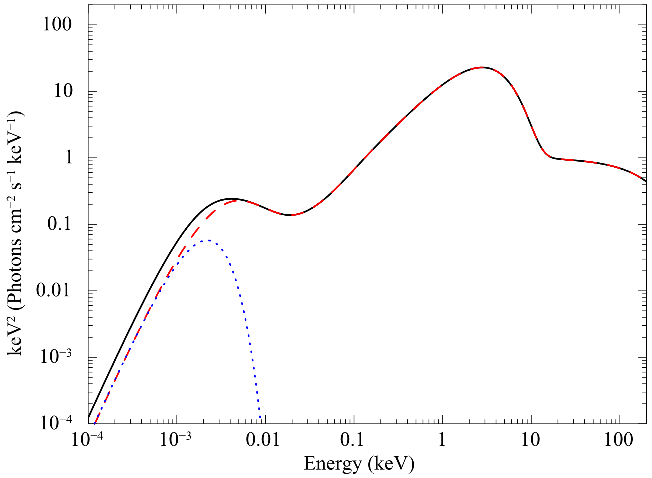

Figure 4. Best-fit absorption/extinction-corrected `optxrplir+bbodyrad` model in the normal high/soft state (MJD 53446). The dashed and dotted lines represent the `kerrconv*optxrplir` component (including the irradiated disk emission and the hard tail) and the `bbodyrad` component (the blackbody emission from the companion star), respectively.

3.2.3. SED Fits for the Chandra Epoch in the Hypersoft State

Adopting the resultant parameters, we next apply the `optxrplir` model to the SED on MJD 53461 in the hypersoft state. The right panel of Figure 3 compares the SED of MJD 53461 with the same model of MJD 53446 in the high/soft state, except for the Eddington ratio, which is adjusted to fit the OIR fluxes. This gives a bolometric luminosity of $\approx 0.7\ L_{\rm Edd}$. Since the OIR to X-ray flux ratio became lower on MJD 53461 than that in the normal high soft state (see Figure 1), the model does not fit the X-ray spectrum. We can clearly see that this model overestimates the soft X-ray flux by about one order of magnitude.

The discrepancy seen in the right panel of Figure 3 cannot be explained by absorption in the optically thin wind detected by Miller et al. (2008). We create a photoionized absorption model with XSTAR, employing the continuum spectral model in Miller et al. (2008) with a luminosity changed to 0.7 $L_{\rm Edd}$ as an incident ionizing spectrum, and assuming the density of the wind as the value determined by them, 1×10^{14} cm^{-3}. As the column density and ionization parameter, we adopt representative values in their photoionization models: $N_{\rm H} = 5 \times 10^{23}$ cm^{-2} and $\xi = 10^4$ erg cm s^{-1}. However, we find this ionized absorption reduces only $\lesssim 3\%$ of the soft X-ray flux. Electron scattering in the absorber, which is not accounted for in the XSTAR code, can only decrease 30% of the radiation. The discrepancy is not canceled out by taking into account the decrease of the mass accretion rate in the inner disk region due to the mass loss in the wind. Miller et al. (2008) estimated the wind outflow rate to be ~10% of the mass accretion rate (assuming that the outflow velocity perpendicular to the disk plane is not much higher than the line-of-sight velocity), and in the more recent work by Miller et al. (2015), it was estimated to be ~30% of the mass accretion rate.

One possibility is that the disk wind made irradiation stronger than the normal high/soft state. The difference in the X-ray versus OIR flux ratio is canceled out if $F_{\rm out}$ at the *Chandra* epoch is ~4 times larger than that in the normal high/

soft state. It is difficult for disk winds to produce blackbody radiation by themselves because they normally have much higher temperatures than those in the outer disks and are optically thin for free–free absorption. Instead, they can contribute to the irradiation of the disk by scattering X-ray photons down and enhancing the illumination of the outer disk (Gierliński et al. 2009). In this case, the geometry-dependent factor for irradiation can be expressed as

$$f_{\rm out} \sim \frac{\Omega_{\rm wind}}{2\pi}(1 - e^{-\tau_{\rm es}}), \tag{3}$$

where $\Omega_{\rm wind}$ and $\tau_{\rm es}$ represent the solid angle of the wind and the optical depth for scattering, respectively.

In our case, however, it is unlikely that the OIR fluxes are enhanced by the optically thin magnetic wind. The *Chandra* spectrum predominantly shows absorption features instead of prominent P-Cygni profiles, and hence $\Omega_{\rm wind}$ must be fairly small. In addition, the disk at the location of the magnetic wind ($\sim 10^{9.7}$ cm) has a relatively high temperature and mainly produces photons with much higher energies than those in the OIR bands. The emitting region is too small to substantially contribute to the OIR fluxes. In the above modeling, the OIR fluxes are dominated by the reprocessed emission from the outer edge of the disk at $R_{\rm out} = 4.4 \times 10^{11}$ cm, where the temperature is $\approx$1 eV. Using the radial dependence of the temperature in the irradiated disk, $T_{\rm irr} \propto r^{-3/7}$ (Cunningham 1976; Veledina et al. 2013), we estimate the disk temperature at the launching point to be $\approx$7 times larger than that at $R_{\rm out}$. To investigate whether the reprocessed emission from the disk around the wind launching radius can explain the opposite behavior of the OIR and X-ray fluxes, we add a `bbodyrad` component with a temperature of 7 eV to the model for MJD 53446 and compare it with the SED at the *Chandra* epoch. We find that the OIR flux levels cannot be reproduced unless we assume an unusually large solid angle at the launching point (more than two orders of magnitude larger than that of the disk).

Moreover, it is difficult for an enhanced $F_{\rm out}$ alone to explain the trend in the soft X-ray spectrum: the inner disk temperature was not largely changed, while the observed X-ray flux was reduced. If the decline of the X-ray flux were produced simply by the decrease of the mass accretion rate in the inner disk region, the temperature should be reduced as well. Considering all the above discussion, we conclude that an optically thin wind is unlikely to be the main cause of the differences in SED between the normal high/soft state and the hypersoft state.

Instead, it seems more likely that obscuring gas is present between the X-ray and optical emission regions, reducing the intrinsic X-ray spectrum. The gas is likely to be very highly ionized and affect the X-ray radiation by Compton scattering, otherwise heavy absorption by less ionized material should modify the spectral shape in the soft X-ray band, inconsistent with the fact that it was kept almost constant in the hypersoft state (see Section 2). Thus, the origin of the gas could be a Compton-thick, equatorial disk wind, strongly scattering out the X-ray photons from the line of sight.

We then fit the multi-wavelength SED at the *Chandra* epoch using the soft thermal Comptonization component implemented in `optxrplir` to extract quantitative information about the observed very steep power-law tail and to obtain a better SED model. We assume that the X-ray flux is scattered by an almost fully ionized, Compton-thick wind, while the OIR emission regions are located outside of the wind. Under the presence of such a wind, it is difficult to predict whether $F_{\rm out}$ becomes larger or smaller than that in the normal high/soft state, or whether it remains constant. If the wind extends rather homogeneously over the outer disk region, the geometry-dependent factor $f_{\rm out}$ increases to $\sim\Omega_{\rm wind}(1 - e^{-\tau_{\rm es}})/(2\pi)$ due to scattering in the wind. If the electron density is the highest at the wind launching point located at a much smaller radius than the outer edge, and if scattering predominantly occurs there, the wind reduces the X-ray photons illuminating the outer disk by $\sim e^{-\tau_{\rm es}}$. The optxrplir model uses the intrinsic X-ray luminosity to calculate the irradiated disk spectrum, and the decrease in illuminating photons is regarded as a decrease in $f_{\rm out}$. Here, we simply assume that $F_{\rm out}$ is not largely changed and use the same value in the high/soft state.

We fixed the parameters, a_* and $a_{\rm out}$ at the values determined in the spectral analysis of the normal high/soft state, and allowed the Eddington ratio and the parameters for the soft thermal Comptonization, $R_{\rm cor}$, $kT_{\rm e}$, and τ to vary. The power-law component is switched off by setting $R_{\rm pl}$ to less than the ISCO. To consider the observed ionized absorption in the wind, we utilize the photoionized absorption model created above, leaving the ionization parameter and column density as free parameters. The `cabs` model is also incorporated to account for the effect that the dense wind (including both fully and partially ionized gas) scatters the X-ray photons out of the line of sight. We linked the column density of `cabs` to that of the photoionized absorption model. The final fit model is `tbabs*xabs*cabs*redden*(kerrconv*optxrplir + bbodyrad)`, where `xabs` represents the photoionized absorption model. The `xabs*cabs` and `redden` components are turned off for the OIR and X-ray data, respectively, by fixing the column densities and reddening factor to negligibly small values.

The condition that we try to model is quite complicated. We simply approximate the observed steep power-law component by the soft thermal Comptonization component included in the `optxrplir` model. It assumes that the seed photons originate in the disk blackbody emitted from the inner disk region at radii within $R_{\rm cor}$ and that they are scatted by a one-zone cloud with given τ and $kT_{\rm e}$. However, the real location, geometry, and internal structure of the Comptonized plasma are unknown. The origin of that component could be a dense corona or a hot flow located in the X-ray-emitting region, or perhaps a Compton-thick disk wind in the outer disk region that strongly down-scatters X-ray photons and modifies the intrinsic spectral shape (see Section 4). Thermal Compton scattering in an optically thick cloud with arbitrary structures has not been prepared as an XSPEC model, and it is difficult to fit the SED directly with realistic models. Moreover, we use one-zone homogeneous ionized absorption and scattering models to describe the disk wind, but the real structure would be more complex. The main purpose of this analysis is not obtaining the precise values of the fit parameters, but investigating whether and how much optically thick Compton scattering can reconcile the huge discrepancy shown in Figure 3. Numerical calculation of radiative transfer employing various structures of the Comptonized cloud and disk wind would be needed for more detailed studies, which is beyond the scope of this article. We leave that to future work.

We find that the multi-wavelength SED can be characterized by the above model consisting of a disk with a luminosity of

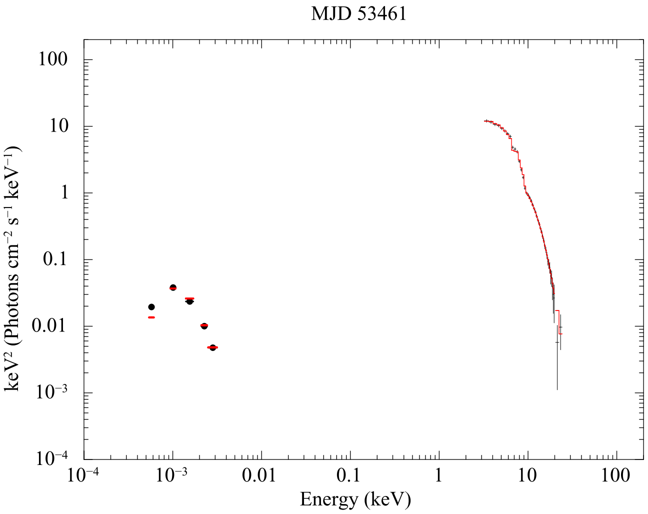

Figure 5. Application of the `optxrplir` model with the soft thermal Comptonization component to the SED on MJD 53461. The bottom panel shows the data vs. model ratio.

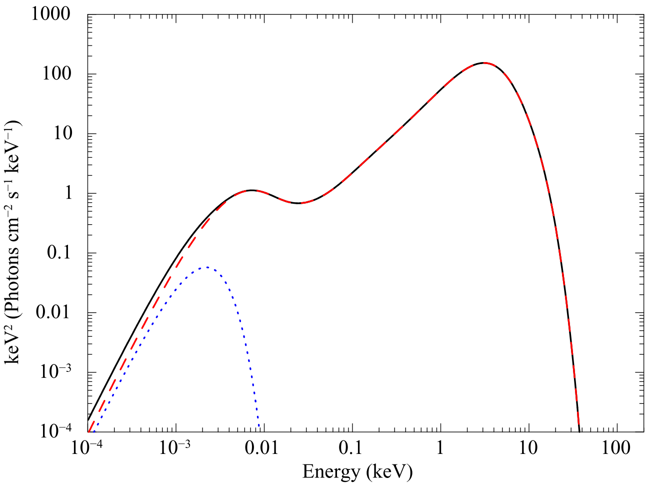

Figure 6. Model presented in Figure 5, corrected for neutral and ionized X-ray absorption, effects of Compton scattering produced by `cabs`, and optical extinction. Dashed and dotted lines represent the `kerrconv*optxrplir` and `bbodyrad` components, respectively.

$L/L_{\rm Edd} \approx 0.74$ and an optically thick, low-temperature Comptonization with $\tau \approx 5.3$ and $kT_{\rm e} \approx 1.4$ keV. Figure 5 plots the comparison of the data and the model, and Figure 6 presents the same model corrected for neutral/photoionized absorption and extinction. The column density of the `cabs` and `xabs` model is estimated to be $\approx 3.0 \times 10^{24}$ cm^{-2} and ξ of the photoionized absorber is $\sim 10^4$ erg cm s^{-1}. In this analysis, we have assumed that the outer disk emission is always seen in the OIR bands without obscuration. It could be partially hidden, however, if an optically thick wind is present between the inner and outer disk regions. In this case, the intrinsic luminosity can be larger and the value estimated above can be regarded as a lower limit. We find that when the normalization of the `kerrconv*optxrplir` component in the OIR bands is set to half of that in the X-ray band, the intrinsic disk luminosity goes up to $\sim 3L_{\rm Edd}$. The model can still reproduce the observed X-ray spectrum by changing $R_{\rm cor}$ (which can be regarded as the strength of the soft thermal Comptonization component) from $26R_{\rm g}$ to 50 $R_{\rm g}$ and the column density of the `xabs` and `cabs` components to 4.5×10^{24} cm^{-2}.

4. DISCUSSION

4.1. The Nature of the Disk Wind in GRO J1655−40

4.1.1. Summary of the Unusual Behaviors

We have revisited the unusual wind detected with *Chandra* from the viewpoint of the long-term spectral and temporal evolutions in the X-ray and OIR bands. A number of peculiar behaviors were found to appear simultaneously in the hypersoft state around the *Chandra* observation, which are summarized as follows.

1. The observed OIR fluxes are monotonically increasing, whereas the X-ray flux starts decreasing before the *Chandra* observation. The *B*-band versus X-ray flux ratio marks the minimal value just around the *Chandra* observation.
2. The observed disk luminosity becomes lower, while the inner disk temperature remains almost the same. The standard $L_{\rm disk} \propto T_{\rm in}^4$ relation appears to break down (Done et al. 2007).
3. The power-law tail seen in the high/soft state spectra is replaced by a low-temperature, optically thick, Comptonized component, while the OIR SED keeps almost the same shape.
4. The absorption feature at ≈8 keV is always seen, and it becomes deeper as the observed X-ray flux decreases (Uttley & Klein-Wolt 2015).
5. Rapid variability is reduced as the observed X-ray flux decreases. The high-frequency break in the X-ray PDS moves downward from ≈5 Hz to ≈0.1 Hz. The break frequency correlates tightly with the observed 3–20 keV flux, while the energy dependence of the PSD shape is not strong (Uttley & Klein-Wolt 2015).

These behaviors become most extreme at around the epoch of the wind detection with the *Chandra*/HETG. If they are not just a coincidence, they would be associated with the disk wind since the ionized absorption feature always seen at ≈8 keV suggests that the wind was steadily present in the hypersoft state.

4.1.2. Interpretation of the Long-term Trend in the X-Ray and OIR Bands

As already discussed, the evolution of the OIR and X-ray fluxes cannot be explained by an increase of the mass accretion rate alone. In this case, the X-ray flux should have monotonically increased as well as the OIR fluxes. The decrease of the X-ray flux is too large to be canceled out by absorption and/or mass loss in the optically thin disk wind detected with *Chandra*. It is also unlikely that an additional contribution from synchrotron emission from jets led to an increase in the OIR fluxes since Migliari et al. (2007) suggest that jets were quenched in the hypersoft state.

One possible interpretation of the high OIR versus X-ray flux ratio in the hypersoft state is that reprocessed emission from the outer disk became stronger than in the normal high/soft state. As discussed in Gierliński et al. (2009), powerful disk winds can enhance the irradiation of the disk. The flux ratio at the *Chandra* epoch could be explained if $F_{\rm out}$, which scales with $f_{\rm out} * (1 - a_{\rm out})$, was ≈4 times larger than that in the normal high/soft state. This means that if $a_{\rm out}$ was constant, $f_{\rm out}$ is 0.4 in the hypersoft state. This value seems somewhat too large, given that no strong emission lines are seen in the *Chandra* spectrum. Instead, a factor of four increase in $F_{\rm out}$ may be achieved if $a_{\rm out}$ decreased somehow in the hypersoft state. It also may be possible that the actual $a_{\rm out}$ and $f_{\rm out}$ values in the normal high/soft state are smaller than what we estimated and that $f_{\rm out}$ increased in the hypersoft state. As explained in Section 3.2.2, we cannot constrain $f_{\rm out}$ and $a_{\rm out}$ simultaneously, and we simply fixed $f_{\rm out}$ at 0.1 in modeling the high/soft state spectrum. However, the launching radius of the wind estimated in Miller et al. (2008) is relatively small and thus its temperature is much higher than that in the outer edge of the disk, around which the OIR photons are emitted (see Section 3.2.3). It is difficult for the disk emission enhanced by that wind to contribute to the OIR fluxes unless we consider an unusually large emitting region.

In addition, the larger $F_{\rm out}$ interpretation alone cannot explain the peculiar behavior of the soft X-ray spectrum in the hypersoft state. If this were the case, the observed X-ray spectrum should directly reflect the intrinsic disk emission, and the trend in the disk luminosity versus inner disk temperature should indicate that the inner disk structure in the hypersoft state is different from that in the high/soft state, in which the inner edge of the standard disk is believed to extend to the ISCO stably (e.g., Ebisawa et al. 1993; Steiner et al. 2010; Shidatsu et al. 2011a). Some previous studies suggest that the disk is truncated at similar luminosities: in the bright low/hard state above $\sim 0.01 L_{\rm Edd}$ (e.g., Done et al. 2007; Shidatsu et al. 2011b; Yamada et al. 2013; Kolehmainen et al. 2014; Shidatsu et al. 2014; Plant et al. 2015) and in the very high state (Tamura. et al. 2012; Hori et al. 2014) over $\sim 0.2 L_{\rm Edd}$ (Kubota & Makishima 2004). However, the properties of the hypersoft state are nothing like these states; the X-ray spectra in the hypersoft state are much softer and the variability power on timescales of ∼0.01–10 s is more than one order of magnitude lower (see, e.g., McClintock & Remillard 2006 and Done et al. 2007 for spectral and timing properties in each state). Moreover, disk truncation in these states produces a larger disk luminosity with a fixed inner temperature, which is the opposite behavior to that observed in the hypersoft state.

Instead, the evolution of the multi-wavelength SED could be better described if $F_{\rm out}$ is not so largely changed between the high/soft and hypersoft states and obscuring gas is present between the inner and outer disk regions, intercepting the line of sight and significantly reducing the observed X-ray luminosity. The obscuring material could be located in an equatorial disk wind. Strong Compton scattering in disk winds can reduce the intrinsic flux significantly when we view them from a high inclination. Recent radiative transfer calculations have suggested that the scattered/reflected component of massive winds significantly contributes to the observed SEDs (Sim et al. 2010a, 2010b). Some observational hints of wind reprocessing have already been found in low-mass X-ray binaries (Díaz Trigo et al. 2012, 2014), implying that broad emission lines, blended with absorption features, could be explained by the reprocessed component of the winds. In our case, however, the Compton-thick part in the wind would be almost completely ionized. Such a wind can scatter out and reduce the intrinsic X-ray photons in the line of sight without changing the spectral shape in the soft X-ray band or generating additional significant atomic absorption and/or emission structures. As shown by our SED analysis in Section 3, this scenario can well explain the unusual trend in the disk spectrum. Using the OIR fluxes as a tracer of the reprocessed luminosity in the outer disk, we have demonstrated that the apparent X-ray flux at the *Chandra* epoch can be $\gtrsim 1$ order of magnitude lower than what is expected.

Similar very soft X-ray spectra with no or only a weak non-thermal power-law component are sometimes observed in other BH low-mass X-ray binaries, such as GRS 1915+105, XTE J1550−564, and GX 339−4 (e.g., Kubota & Makishima 2004; Zdziarski & Gierliński 2004), in their brightest phase. They appear in the luminosity range from $\sim 0.4 L_{\rm Edd}$ to $\sim 1 L_{\rm Edd}$, which is consistent with the luminosity of GRO J1655−40 at the *Chandra* epoch that we estimated in the SED modeling. In previous works, the faint and/or steep power-law tail above ∼10 keV was usually considered to be produced in the inner disk region, and wide-band X-ray spectra in that phase were often reproduced by models composed of the standard disk and its Comptonized corona, or the so-called slim disk model, which describes accretion flows at very high mass accretion rates.

In the case of GRO J1655−40, the scattered-in component of the Compton-thick disk wind could also contribute to the observed Comptonization component. The Compton temperature of the disk wind is estimated to be $T_{\rm C} \sim 1$ keV, by assuming the unabsorbed `optxrplir` model in Figure 6 as the intrinsic spectrum. This is comparable to the electron temperature of the soft Comptonization component. The fairly large difference between the optical depths of the scattered-in component ($\tau \approx 5$, modeled by `optxrplir`) and the scattered out component ($\tau \approx 2$, estimated from the column density of the `cabs` model, $N_{\rm H} = 3 \times 10^{24}$ cm^{-2}), may suggest that different Comptonization components contribute to the soft component. However, considering uncertainties in the spectral modeling, we do not rule out the possibility that the total flux of the soft component is explained by scattering in the disk wind alone. We also note that the irradiated disk emission enhanced by this Compton-thick wind would not contribute greatly to the OIR fluxes. This is because the wind is likely located at a much smaller radius than the outer edge of the disk (see the next section) and the relatively high disk temperature at that position requires a too large solid angle to produce the observed OIR emission (see also Section 3.2.3).

4.1.3. Where is the Hidden Compton-thick Wind Located?

Considering the definition of the ionization parameter, we can constrain the position of the Compton-thick, almost completely ionized part in the disk wind with respect to the less ionized part producing absorption lines. The radial dependence of the ionization parameter is derived from Equation (2) as $\xi(R) \propto 1/(nR^2)$. If the density profile can be written as $n \propto R^{-\alpha}$, a wind is more ionized at larger radii under the condition $\alpha > 2$, while it has the opposite dependence when $\alpha < 2$. The former condition can be established if the disk wind is accelerated in its outer parts. The mass loss rate $\dot{M}_{\rm wind}$ is described as

$$\dot{M}_{\rm wind} \propto R^2 n v_{\rm wind} \Omega, \qquad (4)$$

where Ω and $v_{\rm wind}$ represent the solid angle and velocity of the wind, respectively. A positive radial dependence of the outflow velocity corresponds to $\alpha > 2$, when the mass loss rate and the solid angle are kept constant. Oppositely, the latter condition $\alpha < 2$ can be realized when the wind is decelerated.

The former case means that the Compton-thick region was located at a larger radius than that producing absorption lines, and that the latter part directly perceives the intrinsic X-ray luminosity. The luminosity that we estimated is about 20 times larger than the ionizing X-ray luminosity assumed in the photoionized plasma modeling in previous works. Since the launching radius depends on the square root of the ionizing luminosity (see Equation (2)), it can be larger than that estimated in Miller et al. (2008) by a factor of $\gtrsim 4.4$. In addition, radiation pressure reduces the local effective gravitational force by $(1 - L/L_{\rm Edd}) \lesssim 0.3$, and thereby, the Compton radius is decreased by the same factor. Thus, the two factors can compensate for the order-of-magnitude difference between the wind-launching radius estimated from the *Chandra*/HETG data and the minimum radius at which a thermal wind can be driven. The Compton temperature estimated from our SED model ($T_{\rm C} \sim 1$ keV) gives the critical luminosity $L_{\rm crit} = 0.03 L_{\rm Edd}$, and hence the intrinsic luminosity is sufficiently large to launch a thermal wind.

By contrast, the X-ray photons illuminating the less ionized part of the wind should already be reduced in the latter case, $\alpha < 2$. We suggest this condition would be more plausible than $\alpha > 2$, considering the column density of the scattered-out component ($N_{\rm H} = 3 \times 10^{24}$ cm^{-2}). Approximating the density as $n \sim N_{\rm H} \Delta R$, where ΔR is the size of the Compton-thick part in the line-of-sight direction, and assuming the ionized parameter of that part as $\xi \gtrsim 10^6$ erg cm s^{-1}, we derive

$$R \sim \frac{L_{\rm X}}{N_{\rm H}\xi}\frac{\Delta R}{R} \lesssim 3 \times 10^8 \left(\frac{\Delta R}{R}\right)\left(\frac{L_{\rm X}}{1 L_{\rm Edd}}\right) {\rm cm}. \qquad (5)$$

This value is smaller than the wind-launching radius estimated by Miller et al. (2008). A similar trend in ξ has recently been found in the re-analysis of the *Chandra* data by Miller et al. (2015). From a detailed analysis of the absorption line profile, they detected multiple components in the wind, where a more ionized part was located at a smaller radius.

After Miller et al. (2006) first reported the *Chandra*/HETG result, the unusual wind in GRO J1655−40 has been revisited many times from both observational and theoretical points of view (Netzer 2006; Miller et al. 2008; Kallman et al. 2009; Luketic et al. 2010; Neilsen & Homan 2012; Higginbottom & Proga 2015). Many previous studies were based on the assumption that the wind was optically thin and launched at a few percent of the Eddington luminosity, in constructing photoionized plasma models and performing hydrodynamic simulations. If the wind was Compton-thick and formed at near- or super-Eddington luminosity, the effects of scattering in the wind and radiation pressure should be considered to discuss the wind-driving mechanism. As described above, the launching radius of a thermal-driven wind is smaller at a higher luminosity because radiation pressure reduces the effective gravity. A radiation-pressure-driven wind can be launched at even smaller radii above Eddington luminosity. Further numerical simulations and radiation transfer calculations at high mass accretion rates, including the effects of Compton scattering, would be needed to test whether a Compton-thick, almost completely ionized wind can be really launched and reproduce the observed properties.

4.1.4. X-Ray Short-term Timing Properties

Similar hypersoft X-ray spectra are sometimes detected in the high-mass X-ray binary Cyg X-3 as well (Koljonen et al. 2010; see Uttley & Klein-Wolt 2015 for comparison of the two sources). This system always exhibits peculiar spectral states and lacks rapid variability on shorter timescales than ∼0.1 Hz. Zdziarski et al. (2010) succeeded in describing spectral shapes and the timing properties in Cyg X-3 by considering Compton-thick scattering plasma, likely formed by dense stellar winds from its Wolf–Rayet companion star, with a low temperature (3 keV) and a large optical depth ($\tau \sim 7$) like those of the observed thermal Comptonization component in GRO J1655−40. They found that the break frequency ($\nu_{\rm b}$) in the X-ray PDS is scaled by the size ($R_{\rm scat}$) and the optical depth of the scattering cloud that reduces the intrinsic fast variability, through the following relation:

$$R_{\rm scat} \simeq \frac{c}{2\tau\nu_{\rm b}}. \qquad (6)$$

This could be applied to GRO J1655−40 in the hypersoft state, if its low break frequency is caused by scattering in the Compton-thick disk wind. Using the optical depth for scattering in the line of sight ($\tau \sim 2$) and the break frequency (0.1 Hz) at the *Chandra* epoch, we derive the size of the scattering gas to be $R \sim 10^5 R_{\rm g} \approx 10^{11}$ cm, corresponding to $\sim 0.2 R_{\rm C}$. This value is much larger than the radius of the Compton-thick wind estimated in Section 4.1.3 and appears to favor a different interpretation that the Compton-thick gas extends to the outermost disk region. We note, however, that there are other possible explanations for the suppression of the short-term X-ray variations in the hypersoft state. As discussed in Uttley & Klein-Wolt (2015), the PDS profile may be generated by the intrinsic variation of the accretion flow or variable scattering in the wind due to density inhomogeneities (see Section 4.3).

4.2. A Previously Detected Wind in GRO J1655−40

A similar or more extreme disk wind might be observed in a previous outburst as well. The first detection of ionized absorption lines in GRO J1655−40 was by the *Advanced Satellite for Cosmology and Astrophysics* (*ASCA*; Tanaka et al. 1994) in the outburst starting in 1994 (Ueda et al. 1998). Ionized Fe–K absorption lines were detected in two epochs when the source exhibited similar X-ray continuum spectra but had different observed X-ray fluxes by about one order of magnitude. The ionized absorber was more ionized when the source was brighter, as was seen in the 2005 outburst (Díaz Trigo et al. 2007; Neilsen & Homan 2012). The observed X-ray flux in the *Chandra* observation falls between those at the two epochs reported by Ueda et al. (1998).

A sudden flux drop was detected in the *ASCA* observation at the lower flux (in 1994 August). The duration of the event was several hours, which was much longer than those observed in different periods (on timescales of seconds or minutes; Kuulkers et al. 1998; Shaposhnikov et al. 2007). Interestingly, in this “dip” event, the source kept almost the same continuum shape as outside it, unlike normal absorption dips in low-mass X-ray binaries, which accompany spectral hardening (e.g., Kuulkers et al. 1998, 2013; Homan et al. 2005; Díaz Trigo et al. 2006; Shidatsu et al. 2013). In the dipping period, the ionized Fe–K absorption lines disappeared, while a deep absorption edge appeared at ≈7 keV. This spectral behavior, which was described with double partial-covering absorbers in Tanaka et al. (2003), is reminiscent of the behavior during the hypersoft state in the 2005 outburst. The similarity might suggest that the unusual "dip" event was produced by absorption and scattering in a more extreme wind with an even larger column density and a lower ionization parameter than that observed in 2005 and that a large fraction of the intrinsic X-ray photons was scattered out in the wind. There is, however, no information about the spectral shape in the hard X-ray band above 10 keV for the *ASCA* data, hampering further comparison.

4.3. Implications for Disk Winds in Other Luminous X-Ray Binaries

If these peculiar behaviors in GRO J1655−40 seen around the *Chandra* observation are indeed attributed to an optically thick disk wind launched at a luminosity close to the Eddington limit, they would carry important implications for massive winds thought to be formed at extreme mass accretion rates. Recent radiation (magneto-)hydrodynamic simulations predict radiation-pressure-dominated, optically thick disk winds to be driven in supercritical accretion disks (e.g., Ohsuga et al. 2005; Dotan & Shaviv 2011; Ohsuga & Mineshige 2011). Although the ionized Fe–K absorption lines like those observed in Galactic BH binaries have never been observed in ultraluminous X-ray sources (ULXs; Walton et al. 2012, 2013), Middleton et al. (2014) argued that uneven spectral structures often seen at ≈1 keV could be explained by broad blueshifted absorption lines. Recent deep optical spectroscopy revealed that the broad emission lines of H and He observed in ULXs (and also SS 433, which is the only known Galactic X-ray binary thought to power persistent supercritical accretion; see Fabrika 2004 and references therein) likely originate in dense, strong winds launched on supercritical accretion disks (Fabrika et al. 2015).[7] Moreover, Gladstone et al. (2009) suggest that massive optically thick winds could be the origin of the soft Comptonization component usually detected in ULXs. This component has a low temperature (≈3 keV) and a large optical depth ($\tau \approx 5$–30), similar to those estimated for the thermal Comptonization component in GRO J1655−40. Thus, the unusual GRO J1655−40 wind, formed at around the Eddington luminosity, may be smoothly connected to massive outflows from supercritical accretion flows. More recently, Soria & Kong (2015) and Urquhart & Soria (2015) have proposed a unified picture of the ULXs and the ultraluminous supersoft X-ray sources (ULSs, whose spectra are dominated by a blackbody-like component with a temperature of <0.1 keV and have no hard tail) in terms of the effective optical depth ($\tau_{\rm eff}$)of the supercritical winds: in ULSs, the winds are effectively optically thick and we see only a blackbody emission, while ULX winds are optically thick to Compton scattering but $\tau_{\rm eff} \lesssim 1$, and thus produce a Comptonized component in the X-ray band. We note that $\tau_{\rm eff} \ll 1$ in the case of GRO J1655−40, when a temperature of ∼1 keV and a density of $\sim 10^{16}$ cm^{-3} are assumed to estimate the opacity of free–free absorption in the wind.

Recent simulations by Takeuchi et al. (2013) demonstrated that the winds driven by supercritical accretion have a clumpy structure, that can generate variability. Spectral/flux variation in ULXs that could be explained by the clumpy disk winds has been observed on various wavelengths and timescales, such as X-ray flux on a timescale of several tens of seconds (Middleton et al. 2011) and optical emission lines on $\lesssim 1$ day timescales (Fabrika et al. 2015). As pointed out by Uttley & Klein-Wolt (2015), the clumpiness of the wind may contribute to the observed evolution of high-frequency variability in GRO J1655−40. If the disk wind has a Keplerian velocity in the rotating direction, 0.1 s and 10 s variations correspond to the blob sizes of $10R_{\rm g}$ and $10^2R_{\rm g}$ located at $10^4R_{\rm g}$, respectively. If the bend in the X-ray PDSs is produced by the absorption and scattering in a clumpy wind, variability at a lower frequency is generated by blobs with a larger size and/or located at a larger radius on the disk. In this case, the wind in the *Chandra* observation should have the largest blobs or be located at the most outer region during the hypersoft state, although it is not clear what the mechanisms are that caused the change in geometry and/or inner structures of the wind.

Wind absorption and scattering may also significantly affect the spectra of normal Galactic BH X-ray binaries when they get close to the Eddington luminosity. At high luminosities, the dependence of the disk luminosity ($L_{\rm disk}$) on the inner disk temperature ($T_{\rm in}$) in the high/soft state start departing from the $L_{\rm disk} \propto T_{\rm in}^4$ track for the untruncated standard disk (see Done et al. 2007). High inclination sources with absorption dips and winds, including GRO J1655−40 and 4U 1630−47, deviate downward from the relation in the $L_{\rm disk}$ versus $T_{\rm in}^4$ plane with increasing luminosity, while low inclination systems like GX 339−4 and LMC X-3 do not show such a bend but sometimes go slightly upward. This apparent inclination-dependent discrepancy might be associated with optically thick disk winds and explained as follows: in high inclination sources, we see the inner disk region through the disk wind, and the intrinsic X-ray emission is reduced due to scattering out of the line of sight. In contrast, lower inclination sources have a larger contribution of components scattered into the line of sight, which enhances the X-ray emission from the inner disk region. Moreover, Compton down-scattering in the wind could decrease the observed inner disk temperature. If this is the case, the winds should be almost fully ionized, otherwise significant emission and absorption lines could be seen in low and high inclination systems, respectively. The intrinsic luminosity at the *Chandra* epoch, which we estimated, is consistent with the energy range in which the deviation is seen in other systems, and the GRO J1655−40 wind may be linked to that behavior as an extreme case.

5. CONCLUSION

In this article, we proposed the possibility that the unusual wind in GRO J1655−40 was Compton-thick and almost completely ionized. We demonstrated that the multi-wavelength SED can be reproduced by considering the effects of scattering in the wind. We found that the intrinsic luminosity could be close to or above Eddington, which is much higher than that inferred from the observed X-ray flux. If this is the case, Compton heating and radiation pressure could be more important to driving the wind. To test this possibility, detailed radiation transfer calculation should be made by fully taking into account the effects of scattering in the wind.

We note a paper by Neilsen et al. (2016), which has appeared very recently. They analyzed X-ray and OIR data of GRO

---

[7] We note that these optical emission lines were emitted from much less ionized gas, presumably located at more distant parts in the winds than the optically thick wind in GRO J1655−40 that we have considered.

J1655–40 obtained in a similar period and drew a similar conclusion to ours that the wind was Compton-thick. Their interpretation is that the wind was much more powerful and launched at a much more extreme mass accretion rate (~30 times as high as the Eddington rate) than that in our interpretation, and that most of the observed OIR fluxes in the hypersoft state were produced by the emission from the cool photosphere of the wind itself instead of the emission from the irradiated disk. As discussed in Section 3.2.3, the wind in our model is likely to be optically thin for free–free absorption in the OIR bands, but such a dense wind as suggested by Neilsen et al. (2016) may be effectively thick in the OIR bands and generate blackbody emission.

We are grateful to Michelle Buxton and Charles Bailyn for giving us the optical and near-infrared data obtained with the SMARTS. We thank Roberto Soria, Kazuo Makishima, and Joey Neilsen for fruitful discussions, and the anonymous referee for useful comments that helped to improve the paper. M.S. acknowledges support by the Special Postdoctoral Researchers Program at RIKEN. C.D. acknowledges STFC support from grant ST/L00075X/1. This work is partly supported by a Grant-in-Aid for JSPS Fellows for Young Researchers (M.S.) and for Scientific Research 26400228 (Y.U.). This research has made use of data obtained from the High Energy Astrophysics Science Archive Research Center (HEASARC), provided by NASA's Goddard Space Flight Center.

REFERENCES

Begelman, M. C., McKee, C. F., & Shields, G. A. 1983, ApJ, 271, 70
Bohlin, R. C., Savage, B. D., & Drake, J. F. 1978, ApJ, 224, 132
Boirin, L., & Parmer, A. N. 2003, A&A, 407, 1079
Brenneman, L. W., & Reynolds, C. S. 2006, ApJ, 652, 1028
Buxton, M., & Bailyn, C. 2004, ApJ, 615, 880
Buxton, M., Bailyn, C., & Maitra, D. 2005, ATel, 418, 1
Corbel, S., & Fender, R. P. 2002, ApJL, 573, L35
Coriat, M., Corbel, S., Buxton, M. M., et al. 2009, MNRAS, 400, 123
Cunningham, C. 1976, ApJ, 208, 534
Díaz Trigo, M., & Boirin, L. 2013, AcPol, 53, 659
Díaz Trigo, M., Migliari, S., Miller-Jones, J. C. A., & Guainazzi, M. 2014, A&A, 571, 76
Díaz Trigo, M., Parmar, A. N., Miller, J., Kuulkers, E., & Caballero-García, M. D. 2007, A&A, 462, 657
Díaz Trigo, M., Parmar, J., Boirin, L., Méndez, M., & Kaastra, J. S. 2006, A&A, 445, 179
Díaz Trigo, M., Sidoli, L., Boirin, L., & Parmar, A. N. 2012, A&A, 543, 50
Done, C., Davis, S. W., Jin, C., Blaes, O., & Ward, M. 2012, MNRAS, 420, 1848
Done, C., Gierliński, M., & Kubota, A. 2007, A&ARv, 15, 1
Done, C., Jin, C., Middleton, M., & Ward, M. 2013, MNRAS, 434, 1955
Dotan, C., & Shaviv, N. J. 2011, MNRAS, 413, 1623
Ebisawa, K., Makino, F., Mitsuda, K., et al. 1993, ApJ, 403, 684
Fabrika, S. 2004, ASPRv, 12, 1
Fabrika, S., Ueda, Y., Vinokurov, A., Sholukhova, O., & Shidatsu, M. 2015, NatPh, 11, 551
Frontera, F., Palazzi, E., Zdziarski, A. A., et al. 2001, ApJ, 546, 1027
Gandhi, P., Dhillon, V. S., Durant, M., et al. 2010, MNRAS, 407, 2166
Gierliński, M., Done, C., & Page, K. 2008, MNRAS, 388, 753
Gierliński, M., Done, C., & Page, K. 2009, MNRAS, 392, 1106
Gladstone, J. C., Roberts, T. P., & Done, C. 2009, MNRAS, 397, 1836
Greene, J., Bailyn, C. D., & Orosz, J. A. 2001, ApJ, 554, 1290
Higginbottom, N., & Proga, D. 2015, ApJ, 807, 107
Hjellming, R. M., & Rupen, M. P. 1995, Natur, 375, 464
Homan, J., Miller, J. M., Wijnands, R., et al. 2005, ApJ, 623, 383
Hori, T., Ueda, Y., Shidatsu, M., et al. 2014, ApJ, 790, 20
Hynes, R. I., Haswell, C. A., Cui, W., et al. 2003, MNRAS, 345, 292
Ibragimov, A., Poutanen, J., Gilfanov, M., Zdziarski, A. A., & Shrader, C. R. 2005, MNRAS, 362, 1435
Kallman, T. R., Bautista, M. A., Goriely, S., et al. 2009, ApJ, 701, 865
Kolehmainen, M., Done, C., & Díaz Trigo, M. 2014, MNRAS, 437, 316
Koljonen, K. I. I., Hannikainen, D. C., McCollough, M. L., Pooley, G. G., & Trushkin, S. A. 2010, MNRAS, 406, 307
Kotani, T., Ebisawa, K., Dotani, T., et al. 2000, ApJ, 539, 413
Kubota, A., Dotani, T., Cottam, J., et al. 2007, PASJ, 59, 185
Kubota, A., & Makishima, K. 2004, ApJ, 601, 428
Kuulkers, E., Kouveliotou, C., Belloni, T., et al. 2013, A&A, 552, 32
Kuulkers, E., Wijnands, R., Belloni, T., et al. 1998, ApJ, 494, 753
Luketic, S., Proga, D., Kallman, T. R., Raymond, J. C., & Miller, J. M. 2010, ApJ, 719, 515
McClintock, J. E., & Remillard, R. A. 2006, in Compact Stellar X-Ray Sources, ed. W. H. G. Lewin, & M. van der Klis (Cambridge: Cambridge Univ. Press), 157
Middleton, M. J., Roberts, T. P., Done, C., & Jackson, F. E. 2011, MNRAS, 411, 644
Middleton, M. J., Walton, D. J., Roberts, T. P., & Heil, L. 2014, MNRAS, 438, L51
Migliari, S., Tomsick, J. A., Markoff, S., et al. 2007, ApJ, 670, 610
Miller, J. M., Fabian, A. C., Kaastra, J. S., et al. 2015, ApJ, 814, 87
Miller, J. M., Mineshige, S., Kubota, A., et al. 2014, "ASTRO-H White Paper—Stellar-Mass Black Holes", arXiv:1412.1173
Miller, J. M., Raymond, J., Fabian, A. C., et al. 2006, Natur, 441, 953
Miller, J. M., Raymond, J., Reynolds, C. S., et al. 2008, ApJ, 680, 1359
Nakahira, S., Koyama, S., Ueda, Y., et al. 2012, PASJ, 64, 13
Neilsen, J., & Homan, J. 2012, ApJ, 750, 27
Neilsen, J., & Lee, J. C. 2009, Natur, 458, 481
Neilsen, J., Rahoui, F., Homan, J., & Buxton, M. 2016, arXiv:1603.04070
Neilsen, J., Remillard, R. A., & Lee, J. C. 2011, ApJ, 737, 69
Netzer, H. 2006, ApJ, 652, 117
Novikov, I. D., & Thorne, K. S. 1973, in Black Holes, ed. C. Dewitt, & B. S. Dewitt (New York: Gordon and Breach), 343
Ohsuga, K., & Mineshige, S. 2011, ApJ, 736, 2
Ohsuga, K., Mori, M., Nakamoto, T., & Mineshige, S. 2005, ApJ, 628, 368
Orosz, J. A., & Bailyn, C. D. 1997, ApJ, 477, 876
Plant, D. S., Fender, R. P., Ponti, G., Muñoz-Darias, T., & Coriat, M. 2015, A&A, 573, 120
Ponti, G., Fender, R. P., Begelman, M. C., et al. 2012, MNRAS, 422, L11
Poutanen, J., & Veledina, A. 2014, SSRv, 183, 61
Poutanen, J., Veledina, A., & Revnivtsev, M. G. 2014, MNRAS, 445, 3987
Russell, D. M., Fender, R. P., & Jonker, P. G. 2007, MNRAS, 379, 1108
Shahbaz, T., Charles, P. A., & King, A. R. 1998, MNRAS, 301, 382
Shahbaz, T., van der Hooft, F., Casares, J., Charles, P. A., & van Paradijs, J. 1999, MNRAS, 306, 89
Shaposhnikov, N., Swank, J., Shrader, C. R., et al. 2007, ApJ, 655, 434
Shidatsu, M., Ueda, Y., Nakahira, S., et al. 2011a, PASJ, 63, 803
Shidatsu, M., Ueda, Y., Nakahira, S., et al. 2013, ApJ, 779, 26
Shidatsu, M., Ueda, Y., Tazaki, F., et al. 2011b, PASJ, 63, 785
Shidatsu, M., Ueda, Y., Yamada, S., et al. 2014, ApJ, 789, 100
Sim, S. A., Miller, L., Long, K. S., Turner, T. J., & Reeves, J. N. 2010, MNRAS, 404, 1369
Sim, S. A., Proga, D., Miller, L., Long, K. S., & Turner, T. J. 2010, MNRAS, 408, 1396
Soria, R., & Kong, A. K. H. 2016, MNRAS, 456, 1837
Steiner, J. F., McClintock, J. E., Remillard, R. A., et al. 2010, ApJL, 718, L117
Sutton, A. D., Done, C., & Roberts, T. P. 2014, MNRAS, 444, 2415
Takahashi, H., Fukazawa, Y., Mizuno, T., et al. 2008, PASJ, 60, 69
Takahashi, T., Mitsuda, K., Kelley, R., et al. 2014, Proc. SPIE, 9144, 25
Takeuchi, S., Ohsuga, K., & Mineshige, S. 2013, PASJ, 65, 88
Tamura., M., Kubota, A., Yamada, S., et al. 2012, ApJ, 753, 65
Tanaka, Y., Inoue, H., & Holt, S. S. 1994, PASJ, 46, L37
Tanaka, Y., Ueda, Y., & Boller, T. 2003, MNRAS, 338, L1
Ueda, Y., Asai, K., Yamaoka, K., Dotani, T., & Inoue, H. 2001, ApJL, 556, L87
Ueda, Y., Honda, K., Takahashi, H., et al. 2010, ApJ, 713, 257
Ueda, Y., Inoue, H., Tanaka, Y., et al. 1998, ApJ, 492, 782
Ueda, Y., Yamaoka, K., & Remillard, R. 2009, ApJ, 695, 888
Urquhart, R., & Soria, R. 2016, MNRAS, 456, 1859
Uttley, P., & Klein-Wolt, M. 2015, MNRAS, 451, 475
van Paradijs, J. 1981, A&A, 103, 140
van Paradijs, J. 1983, in Accretion-Driven Stellar X-ray Sources, ed. W. H. G. Lewin, & E. P. J. van den Heuvel (Cambridge: Cambridge Univ. Press), 189
Veledina, A., Poutanen, J., & Vurm, I. 2013, MNRAS, 430, 3196

Veledina, A., Revnivtsev, M. G., Durant, M., Gandhi, P., & Poutanen, J. 2015, MNRAS, 454, 2855
Walton, D. J., Miller, J. M., Harrison, F. A., et al. 2013, ApJL, 773, L9
Walton, D. J., Miller, J. M., Reis, R. C., & Fabian, A. C. 2012, MNRAS, 426, 473
Wilms, J., Allen, A., & McCray, R. 2000, ApJ, 542, 914
Woods, D. T., Klein, R. I., Castor, J. I., McKee, C. F., & Bell, J. B. 1996, ApJ, 461, 767
Yamada, S., Makishima, K., Done, S., et al. 2013, PASJ, 65, 80
Yamaoka, K., Ueda, Y., Inoue, H., et al. 2001, PASJ, 53, 179
Zdziarski, A. A., & Gierliński, M. 2004, PThPS, 155, 99
Zdziarski, A. A., Misra, R., & Gierliński, M. 2010, MNRAS, 402, 767